International Journal of Nanomedicine

Dovepress
Taylor & Francis Group

Open Access Full Text Article

ORIGINAL RESEARCH

Inhalable TFRC-Targeted Extracellular Vesicles Delivery of siTGF-β1 Alleviates Pulmonary Fibrosis via Dual Inhibition of Ferroptosis and Fibroblast Activation

Huan Liang[1],*, Qin Lang[2,3],*, Zongan Liang[2], Jian Sun[2]

[1]Center of Infectious Diseases, West China Hospital, Sichuan University; West China School of Nursing, Sichuan University, Chengdu, People's Republic of China; [2]Department of Pulmonary and Critical Care Medicine, West China Hospital, Sichuan University, Chengdu, People's Republic of China; [3]Department of Pulmonary and Critical Care Medicine, Sichuan Provincial People's Hospital, School of Medicine, University of Electronic Science and Technology of China, Chengdu, People's Republic of China

*These authors contributed equally to this work

Correspondence: Jian Sun, Email sunjian1981@126.com

Background: Idiopathic pulmonary fibrosis (IPF) is a fatal lung disorder marked by excessive extracellular matrix deposition and limited treatment options. Ferroptosis has emerged as a critical driver of epithelial injury and fibrogenesis, while fibroblast activation further accelerates pathological remodeling. The transferrin receptor (TFRC), aberrantly upregulated in both alveolar epithelial cells and fibroblasts during fibrosis, represents a promising target for precision therapy.

Methods: An engineered extracellular vesicle (EV) platform was developed using human umbilical cord mesenchymal stem cell-derived vesicles (HucMSC-EVs). By conjugating a T7 peptide for TFRC targeting and encapsulating small interfering RNA against transforming growth factor-beta 1 (siTGF-β1) through electroporation, a dual-functional nanocomplex (T7-EV/siTGF-β1) was generated. Its delivery efficiency, molecular effects, and therapeutic outcomes were systematically evaluated in vitro and in bleomycin-induced pulmonary fibrosis mouse models.

Results: T7-EV/siTGF-β1 achieved targeted uptake by epithelial cells and fibroblasts, efficiently silencing TGF-β1 expression. Treatment significantly inhibited iron accumulation, reactive oxygen species (ROS) generation, and lipid peroxidation, thereby suppressing ferroptosis. Concurrently, the nanocomplex reduced myofibroblast activation, collagen deposition, and fibrotic remodeling, ultimately improving lung histopathology and respiratory function. Importantly, aerosolized administration enabled preferential lung accumulation with minimal off-target distribution and excellent biocompatibility.

Conclusion: This study demonstrates that simultaneous inhibition of epithelial ferroptosis and fibroblast activation via TFRC-targeted EV-mediated siRNA delivery effectively mitigates pulmonary fibrosis. T7-EV/siTGF-β1 thus offers a synergistic and clinically translatable strategy for treating IPF and other fibrotic lung diseases.

Plain Language Summary:

- Alveolar epithelial ferroptosis promotes fibroblast activation through TGF-β1 signaling.
- TFRC is upregulated during early-to-mid fibrosis, enabling stage-specific targeted delivery.
- T7-modified MSC-derived EVs exhibit enhanced TFRC-mediated targeting and siRNA delivery.
- T7-EV/siTGF-β1 suppresses ferroptosis and oxidative stress in bleomycin-injured epithelial cells, and inhibits TGF-β1-mediated fibroblast activation in vitro and vivo.

Keywords: extracellular vesicles, T7 peptide, TFRC, ferroptosis, pulmonary fibrosis

---

https://doi.org/10.2147/IJN.S568106
Received: 16 September 2025
Accepted: 23 January 2026
Published: 2 February 2026

Graphical Abstract

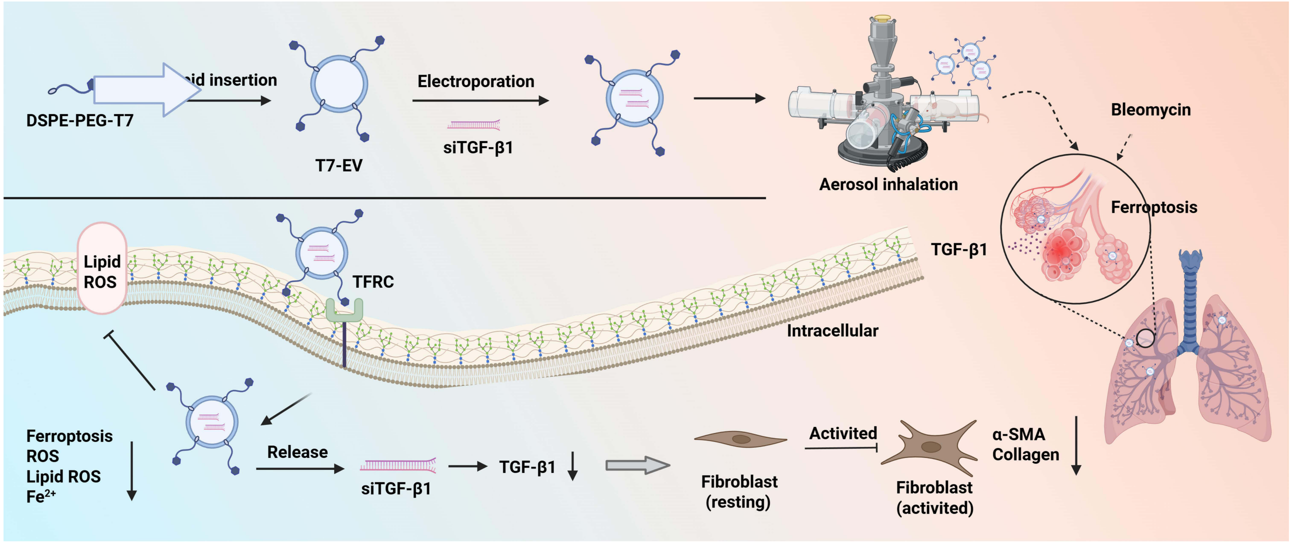

Introduction

Idiopathic pulmonary fibrosis (IPF) is a progressive and fatal interstitial lung disease characterized by excessive deposition of extracellular matrix (ECM), destruction of alveolar architecture, and irreversible loss of pulmonary function.[1,2] Despite the clinical use of antifibrotic agents such as pirfenidone[3] and nintedanib,[4] their efficacy is limited. They only modestly slow disease progression without reversing established fibrosis or significantly improving survival.[5–7] The complex and multi-factorial pathogenesis of IPF-encompassing persistent epithelial injury,[8,9] fibroblast activation,[10] immune dysregulation,[11,12] and metabolic reprogramming,[13,14] underscores the urgent need for more targeted and effective therapeutic strategies.

Emerging evidence has identified ferroptosis, a form of regulated cell death driven by iron-dependent lipid peroxidation,[15,16] as a critical contributor to alveolar epithelial damage,[17] exacerbated inflammation,[18] and fibrotic remodeling in IPF.[19] Dysregulated expression of ferroptosis-associated genes such as GPX4,[20,21] ACSL4,[22] and TFRC,[23] has also been observed in preclinical models or human IPF tissues. In our study, we found that ferroptotic epithelial cells release TGF-β1, which subsequently activates resident fibroblasts and promotes excessive ECM deposition.[24] Moreover, iron overload and oxidative stress within the fibrotic lung further exacerbate ferroptosis, forming a vicious cycle that fuels disease progression.

While ferroptosis inhibitors such as ferrostatin-1 have shown therapeutic promise in animal models,[23] their clinical translation is hindered by poor pharmacokinetic properties, lack of tissue specificity, and systemic toxicity risks.[25] Targeted drug delivery systems offer a potential solution to these challenges. Extracellular vesicles (EVs), particularly those derived from mesenchymal stem cells (MSCs),[26,27] possess inherent biocompatibility, immune evasion capability, and antioxidative activity. They not only exert direct therapeutic effects but also serve as ideal nanocarriers for delivering various therapeutic cargos.[28–31] However, unmodified EVs lack tissue-targeting specificity, limiting their efficiency in fibrotic lungs. Transferrin receptor (TFRC), a membrane protein responsible for iron uptake. During the progression of fibrosis, its expression is abnormally upregulated in both alveolar epithelial cells and fibroblasts, making it a promising molecular target for precise drug delivery. However, targeting TFRC throughout all stages of pulmonary fibrosis may raise concerns, as this disease is closely associated with lung cancer, which is characterized by high TFRC expression. Accordingly, in this study, we first examined the stage-dependent dynamics of TFRC expression during pulmonary fibrogenesis, aiming to define a rational therapeutic window and inform the optimization of TFRC-targeted delivery strategies.

We engineered EVs derived from human umbilical cord MSCs (HucMSCs) with a TFRC-targeting T7 peptide (T7-EV), enabling selective delivery to TFRC-expressing cells in the fibrotic lung.[32,33] We further loaded these EVs with small interfering RNA against TGF-β1 (siTGF-β1), aiming to simultaneously block profibrotic signaling and attenuate ferroptosis. We demonstrated that T7-EV/siTGF-β1 not only protected alveolar epithelial cells from bleomycin-induced ferroptotic damage in vitro but also effectively inhibited fibroblast activation and ECM accumulation. Moreover, aerosolized inhalation of T7-EV/siTGF-β1 significantly alleviated lung fibrosis in vivo, with improved survival and minimal systemic toxicity. These findings highlight the potential of TFRC-targeted, EV-based RNA delivery as a novel strategy for combating ferroptosis-driven pulmonary fibrosis.

Materials and Methods

Cells and Animals

The HucMSC, MLE-12 and NIH3T3 cell lines were obtained from the American Tissue Type Collection (ATCC). Six- to eight-week-old male C57BL/6J mice were purchased from Beijing Vital River Laboratory Animal Technology Co., Ltd. (Beijing, China) and maintained at a constant temperature (25 ± 1 °C).

Materials and Instruments

DMEM culture medium, penicillin-streptomycin (PS) and Fetal bovine serum (Gibco), Bleomycin sulfate, Fer-1 and DFO (MCE), HE staining kit, Masson's staining kit and 0.5% crystal violet staining solution (Yeasen), EPPB enhanced Prussian blue staining kit and FITC-Phalloidin (Solarbio), Transwell (Corning), CCK-8 and 4% PFA (Biosharp), C11-BODIPY581/591 (Merck), RhoNox-1, Deferoxamine (DFO), Bleomycin sulfate and Liproxstatin-1 (MCE), Dihydroethidium (Beyotime), BC-T4 culture medium (Baso), anti-CD34, anti-CD19 and anti-CD45 (BD), anti-CD90, anti-CD73 and anti-CD105 (Biolegend), anti-CD63, anti-Flotillin-1, anti-Calnexin and anti-TGF-β1 (HUABIO), anti-Collagen I (Abcam), anti-TFRC (Abways), anti-α-SMA (Proteintech), Recombinant Mouse/Rat TGF-beta 1 (Novoprotein, Shanghai, China). DSPE-PEG2000-T7 (XINGBEIAIKE). The siRNA targeting mouse TGF-β1 (siTGF-β1) was synthesized with the following sequences: sense, 5′-CGGACUACUAUGCUAAAGATT-3′; antisense, 5′-UCUUUAGCAUAGUAGUCCGTT-3′.

Flow cytometry (NovoCyte, ACEA Biosciences, Agilent Technologies), Confocal microscopy (LSM 980, ZEISS), Electroporator (Gene Pulser Xcell™, Bio-Rad), Mini-extruder for liposomes (1EA, Avanti), High-speed centrifuge (Sorvall LYNX 6000, Thermo Fisher Scientific), Ultrahigh-speed centrifuge (Optima L-100XP, Beckman Coulter), Cell counter (BioLab, Elite Biotechnology Co., Ltd., Shanghai), Nanoparticle tracking analyzer (ZetaView, Particle Metrix), Nasal–oral aerosol inhalation system (AER-6A-MS6, Shanghai Tawong Intelligent Technology Co., Ltd). Small animal in vivo imaging system (IVScope 8000, Clinx).

Cell Culture

MLE-12 and NIH 3T3 cells were cultured in DMEM supplemented with 10% FBS and 1% PS. HucMSCs were expanded in Serum-free medium containing 5% serum substitute at 37 °C in a humidified incubator with 5% CO_2. Unless otherwise specified, ferroptosis in MLE-12 cells was induced by 10 μg/mL bleomycin and treated by 5 μM Ferrostatin-1 (Fer-1) or 5 μM DFO, while NIH 3T3 cells were activated by exposure to 10 ng/mL TGF-β1. Unless otherwise specified, MLE-12 cells were seeded at a density of 0.5×10^4 cells per well in 96-well plates, 3×10^4 cells per well in 24-well plates, and 1×10^5 cells per well in 6-well plates.

Cell Viability Detection

MLE-12 cells were first seeded into 96-well plates. After 24 h, cells were treated with different drugs and incubated for an additional 48 h. Then, 100 μL of CCK-8 working solution was added to each well and incubated at 37°C for 2 h. Absorbance was measured at 450 nm using a microplate reader, and cell viability was calculated accordingly.

Intracellular ROS and Lipid Peroxidation Level

For ROS detection, MLE-12 cells were seeded into 24-well plates. After 24 h, cells were treated with the indicated drugs and incubated for another 48 h. Subsequently, DCFH-DA (1 μM) was added and incubated at 37°C for 30 min. After three washes with PBS, intracellular ROS levels were assessed using fluorescence microscopy and flow cytometry. To assess intracellular lipid peroxidation levels, MLE-12 cells were treated as described above for 48 hs, then washed three times with PBS. Subsequently, 200 μL of C11-BODIPY staining solution (2 μM) was added to each well and incubated at 37°C for 30 minutes. After staining, cells were washed three times with PBS, and lipid peroxidation was evaluated by flow cytometry or confocal microscopy.

Intracellular Fe^{2+} Level

For Fe^{2+} detection, MLE-12 cells were seeded in 24-well plates. After 24 h, cells were treated with the indicated drugs and cultured for another 48 h. Cells were then collected and washed three times with PBS. Each sample was incubated with 200 μL of FeRhoNox-1 staining solution (2 μM) at 37°C for 30 min. After staining, cells were washed three times with PBS, and intracellular Fe^{2+} levels were measured using flow cytometry.

Preparation of Conditioned Medium (CM) from Injured MLE-12

MLE-12 cells were treated with bleomycin or bleomycin combined with other reagents for 48 h. The medium was then replaced with fresh complete DMEM, and cells were cultured for an additional 48 h. The supernatant was collected and centrifuged at 2000 rpm for 10 min at 4 °C to remove cell debris. The resulting supernatant was filtered through a 0.22 μm membrane and subsequently concentrated using Amicon Ultra centrifugal filters with a 3 kDa molecular weight cutoff. The filtrate obtained was used as the CM.

In vivo Fibroblast Activation Assay

A Transwell assay was conducted to assess the migratory capacity of cells. NIH3T3 cells were subjected to different treatments for 48 h before seeding. Subsequently, 100 μL of the treated cell suspension (2×10^6 cells/mL) was added to the upper chamber of a Transwell insert placed in a 24-well plate, while 1 mL of DMEM containing 1% FBS (v/v) was added to the lower chamber. After incubation at 37 °C for 6–8 h, non-migrated cells on the upper surface were removed. The cells that had migrated to the lower surface were then fixed and stained with crystal violet. Migrated cells were visualized and quantified using ImageJ software. Immunofluorescence was used to assess the expression levels of Collagen I and α-SMA. After 48 h, cells were fixed with 4% PFA at room temperature for 20 min, permeabilized with 0.5% Triton X-100 for 5 min, then washed three times with PBS. Cells were incubated with anti-Collagen I or anti-α-SMA antibodies overnight at 4°C, followed by incubation with FITC-labeled secondary antibodies for 1 h at room temperature.

Establishment of a Mouse Model of Pulmonary Fibrosis

Male C57BL/6J mice were acclimated for at least one week before use, and those weighing 28 ± 2 g were selected for modeling. After anesthesia with 1% pentobarbital sodium via intraperitoneal injection, mice were placed in an upright position for endotracheal intubation through the glottis. Bleomycin sulfate (2.5 mg/kg) was slowly administered into the trachea, while control mice received an equal volume (40 μL) of saline. Following administration, mice were gently rotated to ensure even distribution within the lungs.

Histological Analysis

Mice were sacrificed at different time points, and lung tissues were collected and fixed in 4% PFA for at least 48 h before paraffin embedding and sectioning. Prior to performing HE, Masson's staining, immunohistochemical staining for TGF-β1 (1:200 dilution) and α-SMA (1:10,000 dilution), and EPPB-enhanced Prussian blue staining, the sections were deparaffinized and rehydrated.

Assessment of TFRC Expression in vivo

Lung tissue sections were collected from mice on Day 0, 14, and 21 following bleomycin-induced injury. Immunohistochemical staining was performed to evaluate the expression levels of transferrin receptor (TFRC, 1:100 dilution) (n = 3 per time point). In addition, lung tissue sections from patients with idiopathic pulmonary fibrosis (IPF) were analyzed for TFRC expression and compared to adjacent non-tumorous lung tissues from cancer patients, which served as the control group (n = 3).

Assessment of TFRC Expression in vitro

MLE-12 cells were treated with bleomycin for 48 h in 24-well plates, while NIH 3T3 cells were treated with TGF-β1 at concentrations of 0, 5, or 10 ng/mL for 48 h in 24-well plates. After treatment, cells were washed three times with PBS and fixed with 4% paraformaldehyde for 15 min. Subsequently, FITC-conjugated TFRC antibody was added (1:100 dilution), and cells were incubated at 4 °C in the dark for 30 min. TFRC expression was then evaluated by fluorescence microscopy or flow cytometry.

Single-Cell Gene Expression Data Analysis

Single-cell RNA sequencing data from the GSE128033 dataset were analyzed using the Seurat R package. Briefly, raw gene–cell count matrices generated by the 10x Genomics platform were imported into R and processed following standard Seurat workflows. Cells with low gene counts or high mitochondrial gene percentages were excluded to ensure data quality. After normalization and scaling, highly variable genes were identified, and dimensionality reduction was performed using principal component analysis (PCA). Batch effects across samples were corrected using Harmony integration, followed by unsupervised clustering and visualization with Uniform Manifold Approximation and Projection (UMAP). Samples were grouped into three disease stages according to clinical metadata: Normal, Early disease, and Late disease. To compare the expression levels of TFRC across disease stages, TFRC expression was extracted at the single-cell level from the normalized expression matrix. Given the non-normal distribution of single-cell gene expression data, Wilcoxon rank-sum tests were applied to assess differences in TFRC expression between disease groups. Pairwise comparisons were performed among Normal, Early disease, and Late disease groups, and statistical significance was determined using two-sided tests. Violin plots were used to visualize TFRC expression distributions across groups.

HucMSCs Culture and EV Preparation

HucMSCs morphology was monitored by phase-contrast microscopy. Immunophenotypic profiling was carried out by flow cytometry, using antibodies against canonical mesenchymal markers (CD73, CD90, CD105) and against hematopoietic markers (CD19, CD34, CD45) as negative controls. Isotype controls were included (BB515 Mouse IgG1, κ Isotype Control, PE Mouse IgG, κ Isotype Control, and FITC-Mouse IgG, κ Isotype Control) for control samples. All antibodies were used at a dilution of 1:100.

EVs were prepared following a modified protocol based on previously published methods. Briefly, the HucMSCs suspension was passed through a series of polycarbonate membrane filters (1 µm, 0.4 µm, and 0.2 µm pore sizes) using a mini-extruder to ensure uniform vesicle sizing.[34] The resulting suspension was then subjected to centrifugation to isolate EVs. The purified EVs were resuspended in sterile PBS. The morphology, particle size, zeta potential, and marker protein expression of EVs were assessed using transmission electron microscopy (TEM), nanoparticle tracking analysis (NTA), and Western blot, respectively.

Construction of T7-EV

To prepare T7-modified extracellular vesicles (T7-EV), 10 µg of EVs were mixed with DSPE-PEG2000-T7 (T7 peptide: HAIYPRH) at various mass ratios (w/w) of 3:1, 2:1, 1:1, 1:2, and 1:3, and incubated at 37 °C for 1 h. Unbound DSPE-PEG2000-T7 was then removed using size-exclusion chromatography (SEC), yielding purified T7-EV. The fluorescence intensity of DSPE-PEG2000-T7 on the surface of T7-EV was measured using a microplate reader (Molecular Devices ID5). Modification efficiency was calculated as the ratio of the amount of surface-bound material to the total amount initially added.

Loading siRNA in EV or T7-EV by Electroporation

EV or T7-EV were diluted in electroporation buffer to a final concentration of 0.5 µg/µL and mixed with siRNA at a weight ratio of 4:1 (EVs: siRNA). The mixture was incubated on ice for 30 min, then transferred to an electroporation cuvette. Electroporation was performed using a Bio-Rad electroporator with the following settings: capacitance = 125 µF and cuvette gap = 1 mm. After electroporation, the mixture was incubated on ice for another 30 min to allow EV membrane recovery. Free siRNA was removed using size-exclusion chromatography (SEC).

Cytotoxicity Assay

MLE-12 and NIH 3T3 cells were seeded into 96-well plates. After 24 h, cells were treated with EVs, Lipo2000, or T7-EV at concentrations of 0, 6.25, 12.5, 25, 50, and 100 μg/mL. Following an additional 24-h incubation, cell viability was assessed by measuring absorbance at 450 nm using the CCK-8 assay, and cytotoxicity was calculated accordingly.

Assessment of Cellular Uptake Efficiency

MLE-12 and NIH 3T3 cells were seeded in 24-well plates. After 24 h, cells were treated with 0.5 mL of complete medium containing EVs or T7-EV labeled with 10 μg/mL DiR. Following an additional 24-h incubation, cells were collected for flow cytometry analysis to assess uptake efficiency. For confocal microscopy, cells were cultured on coverslips in 24-well plates and treated as described above. After 24 h, cells were fixed and permeabilized as described in In Vivo Fibroblast Activation Assay, then stained with FITC-Phalloidin at room temperature for 30 min, and counter-stained with DAPI for 10 min. After washing, slides were mounted with anti-fade mounting medium and sealed. Images were acquired using confocal microscopy.

Assessment of siRNA Delivery Efficiency

MLE-12 and NIH 3T3 cells were seeded in 24-well plates. After 24 h, cells were treated with Cy3-siRNA (0.5 μg), Lipo2000 combined with Cy3-siRNA (1 μg Lipo2000 + 0.5 μg siRNA per well), or EVs loaded with Cy3-siRNA (2 μg EV + 0.5 μg siRNA per well). For the Lipo2000 group, the transfection was performed in serum-free medium for 6 h, followed by replacement with complete DMEM. In contrast, the EV and T7-EV groups were transfected directly in complete DMEM without medium change. After 24 h of transfection, siRNA delivery efficiency was assessed using flow cytometry and confocal microscopy. Flow cytometry data were analyzed using NovoExpress software (ACEA Biosciences, Agilent Technologies), and confocal images were processed using ZEN 3.4 software (ZEISS).

In vitro Evaluation of T7-EV Targeting Capability

MLE-12 and NIH 3T3 cells were seeded onto cell slides in 24-well plates. After 24 h, the medium was replaced with 500 μL of complete DMEM medium containing PBS, EV+Cy3-siRNA, or T7-EV+Cy3-siRNA (2 μg EV or T7-EV with 0.5 μg siRNA per well), followed by 6 h incubation. After incubation, cells were washed three times with PBS and fixed with 4% PFA for 20 min at room temperature. Following fixation, cells were stained with FITC-conjugated TFRC antibody (1:100 BSA diluted) for 1 h. DAPI staining and slide preparation were performed as described in Assessment of Cellular Uptake Efficiency.

To evaluate the competitive binding of transferrin, MLE-12 and NIH 3T3 cells were pretreated with transferrin at concentrations of 0, 1.25, 2.5, 5.0, and 10.0 mg/mL for 2 h. Subsequently, T7-EV/Cy3-siRNA was added to the cells, and cellular uptake efficiency was assessed by flow cytometry after 24 h.

Lysosomal Escape

MLE-12 and NIH 3T3 cells were seeded onto coverslips in 24-well plates. After 24 h, cells were incubated with T7-EV loaded with Cy3-siRNA for 6 h. For lysosomal colocalization analysis, Lysotracker probe (1:10,000 dilution) was added directly for 2 h. Alternatively, after 8 h of incubation, the medium was replaced with fresh complete DMEM without T7-EV/Cy3-siRNA, and cells were further cultured until 22 h before Lysotracker staining. Following staining, cells were washed with PBS, fixed in 4% PFA for 20 min at room temperature, and counterstained with DAPI for 10 min. Coverslips were mounted with antifade reagent and sealed with nail polish. Images were acquired using confocal laser scanning microscopy.

In vivo Distribution Following Aerosol Inhalation

T7-EV/Cy5-siRNA complexes were administered to C57BL/6 mice via a small-animal nose-only aerosol inhalation system. Each mouse was exposed to aerosolized particles for 30 minutes at a nebulization rate of 0.2 mL/min, with a dose of 10 µg Cy5-siRNA per mouse. Organs including the heart, liver, spleen, lungs, and kidneys were harvested for ex vivo imaging before nebulization and 1 h post-inhalation.

In vivo Therapeutic Efficacy of T7-EV/siTGF-β1

A mouse model of pulmonary fibrosis was established by intratracheal instillation of bleomycin. After modeling, the mice were randomly divided into 4 groups (n = 12): PBS, siTGF-β1, T7-EV/siNC, and T7-EV/siTGF-β1. From Day 3 post-modeling, mice received aerosol inhalation every 3 days for a total of 6 administrations. The dosage was 40 µg T7-EV and 10 µg siRNA per mouse per treatment. Survival status was monitored daily, and body weight was recorded every 3 days. On Day 21, mice were euthanized, and lung tissues were collected for gross morphology, histopathological examination, and immunohistochemical analysis.

Statistical Analysis

All experiments were performed in at least triplicate. Data are presented as means with 95% confidence intervals. Two-group comparisons were analyzed using a two-tailed Student's *t*-test. Comparisons among three or more groups were analyzed using one-way or two-way ANOVA followed by Tukey's post-hoc test. Statistical analyses were conducted in GraphPad Prism v9. P value < 0.05 was considered statistically significant.

Results

Bleomycin-Induced Ferroptosis Upregulates TGF-β1 and TFRC, Contributing to Fibroblast Activation

To determine whether alveolar epithelial cells undergo ferroptosis during pulmonary fibrosis and promote fibroblast activation via TGF-β1 secretion, we first exposed MLE-12 cells to bleomycin (Figure 1A). Bleomycin treatment significantly reduced cell viability and increased intracellular reactive oxygen species (ROS), lipid peroxidation, Fe^{2+} accumulation, and TGF-β1 protein expression. These effects were notably reversed upon treatment with the ferroptosis inhibitor ferrostatin-1 (Fer-1, Figure S1A–D). Western blot analysis further confirmed the upregulation of TGF-β1 in MLE-12 cells following bleomycin exposure (Figure 1B). Conditioned medium (CM) collected from bleomycin-treated epithelial cells significantly enhanced fibroblast migration, which was also reversed by Fer-1 co-treatment (Figure 1C–D).

To validate these findings in vivo, a murine model of pulmonary fibrosis was established via intratracheal administration of bleomycin. Histological analysis using HE and Masson's trichrome staining, along with immunohistochemistry for TGF-β1 and α-SMA, confirmed successful fibrosis induction (Figure S2A–D). Enhanced Perls' Prussian Blue (EPPB) staining revealed a marked increase in iron accumulation that correlated with fibrosis severity, indicating disrupted iron homeostasis and ferroptosis in fibrotic lung tissues (Figure S2C–D). These findings support the concept that targeting ferroptosis and subsequent fibroblast activation may represent a promising therapeutic strategy for pulmonary fibrosis.

Next, we assessed the expression of TFRC, a key gene involved in iron uptake, by IHC in lung tissues of fibrotic mice. TFRC expression was significantly elevated on Day 14 after bleomycin instillation but declined to near-normal levels by Day 21 (Figure 1E).

Next, we evaluated TFRC expression by immunohistochemistry in lung tissues from patients with idiopathic pulmonary fibrosis (IPF). Based on the extent of fibrosis, IPF lung samples were stratified into early-stage and late-stage groups. TFRC-positive cells were significantly increased in early-stage IPF lungs compared with control tissues, whereas TFRC expression was markedly reduced in late-stage IPF lungs (Figure 1F and S3A–B). Analysis of IPF-related single-cell datasets from public databases further confirmed a consistent trend in TFRC mRNA expression changes (Figure 1G). This dynamic pattern is consistent with our observations in the bleomycin-induced fibrotic mouse model, suggesting that TFRC is transiently upregulated during the active phase of fibrotic progression but downregulated at late stages.

In vitro, bleomycin-treated MLE-12 cells also showed increased TFRC expression (Figure 1H–I). Similarly, the proportion of $TFRC^{+}$ NIH 3T3 fibroblasts was significantly increased following TGF-β1 stimulation (Figure 1J). Collectively, these data suggest that TFRC may serve as a potential target for delivering anti-ferroptotic and anti-fibrosis agents during the active phase of pulmonary fibrosis.

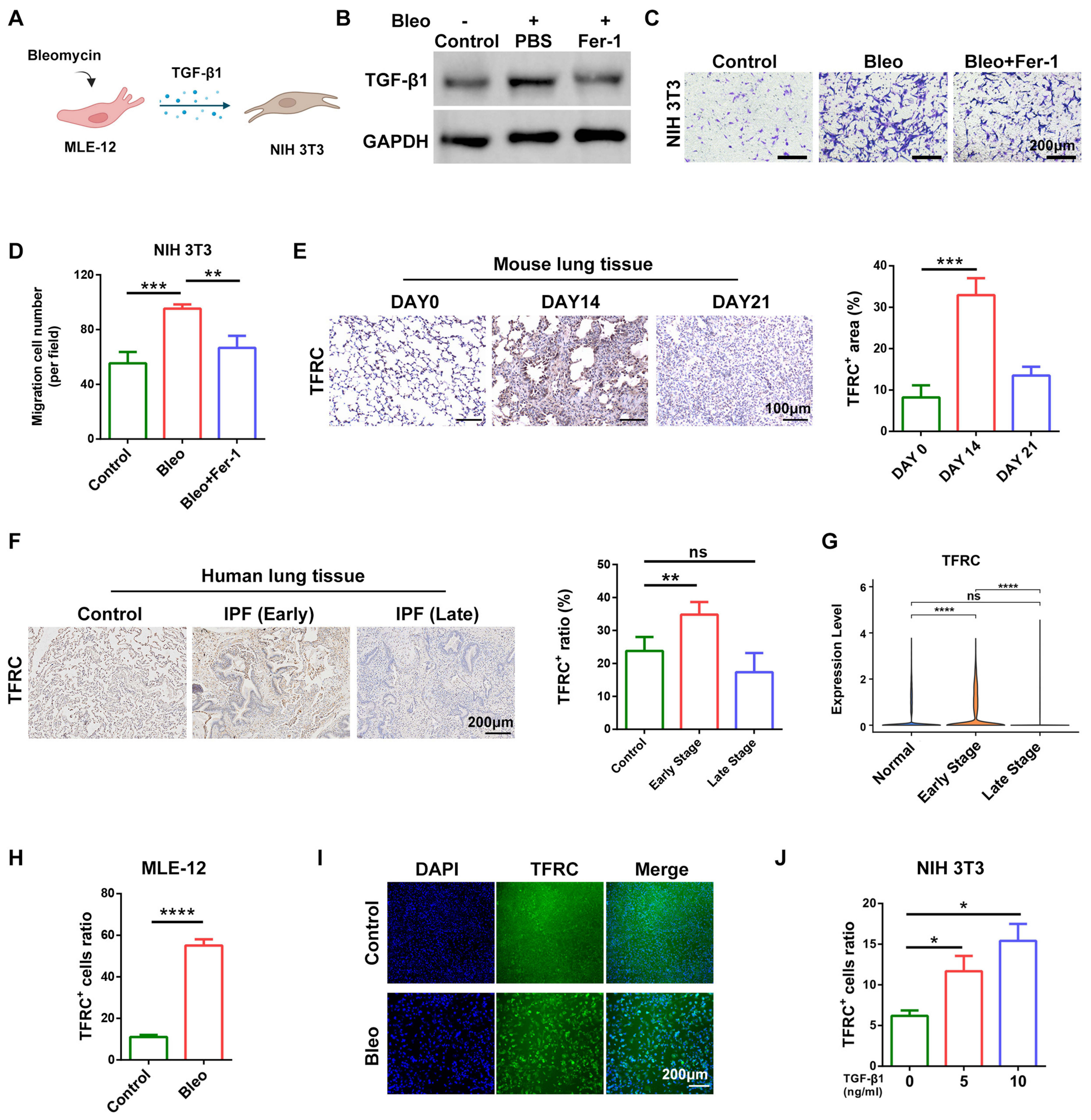

Figure 1 Bleomycin-induced ferroptosis upregulates TGF-β1 and TFRC, contributing to fibroblast activation. (**A**) The schematic illustrates that bleomycin induces ferroptosis and aberrant TGF-β1 expression in MLE-12 cells, which in turn activates fibroblasts. (**B**) Western blot analysis of TGF-β1 expression in MLE-12 cells treated with bleomycin or bleomycin combined with Fer-1. (**C**) Conditioned medium (CM) from MLE-12 cells treated with bleomycin or bleomycin + Fer-1 was collected and used to culture NIH 3T3 cells. The migratory ability of NIH 3T3 cells was assessed by Transwell assay. (**D**) Quantification of NIH 3T3 cell migration from the Transwell assay. (**E**) TFRC expression in mouse lung tissues on days 0, 14, and 21 after bleomycin administration, with statistical analysis. (**F**) Representative images of IHC staining for TFRC in IPF patients. (**G**) Quantitative analysis of IHC staining results. (**H**) Flow cytometric analysis of the proportion of TFRC-positive MLE-12 cells after bleomycin induction. (**I**) Fluorescence microscopy images showing TFRC-positive MLE-12 cells after bleomycin treatment. (**J**) Flow cytometric analysis of the proportion of TFRC-positive NIH 3T3 cells following stimulation with 0, 5, and 10 ng/mL TGF-β1. Data are presented as the mean ± SD. *$P < 0.05$, **$P < 0.01$, ***$P < 0.001$, ****$P < 0.0001$.

Preparation and Characterization of T7-EV

The T7 peptide has been well characterized for its specific affinity to TFRC and is widely utilized for targeted modification in a variety of nanoparticle-based delivery systems. While MSCs–derived EV exhibit potent antioxidant properties, their therapeutic efficacy is often limited by a lack of intrinsic targeting capability. Based on this, we employed DSPE-PEG2000-T7 to modify EV derived from HucMSCs, aiming to impart TFRC-targeting capability (Figure 2A). The HucMSCs used for EV preparation were characterized according to international standards. Morphologically, the cells exhibited a spindle-shaped appearance under the microscope. Flow cytometry analysis showed that the expression levels of CD73, CD90, and CD105 were all above 98%, while the levels of CD19, CD34, and CD45 were below 1%, meeting the established criteria (Figure S4A-B). According to the standard curve of FITC-labeled DSPE-PEG2000-T7, the optimal modification efficiency was achieved at an EV: DSPE-PEG2000-T7 mass ratio of 1:1, reaching 49.45 ± 0.82% (Figure 2B and S5A). Transmission electron microscopy showed that both unmodified EV and T7-EV maintained a characteristic cup-shaped morphology, with average diameters of 169.5 nm and 160.1 nm,

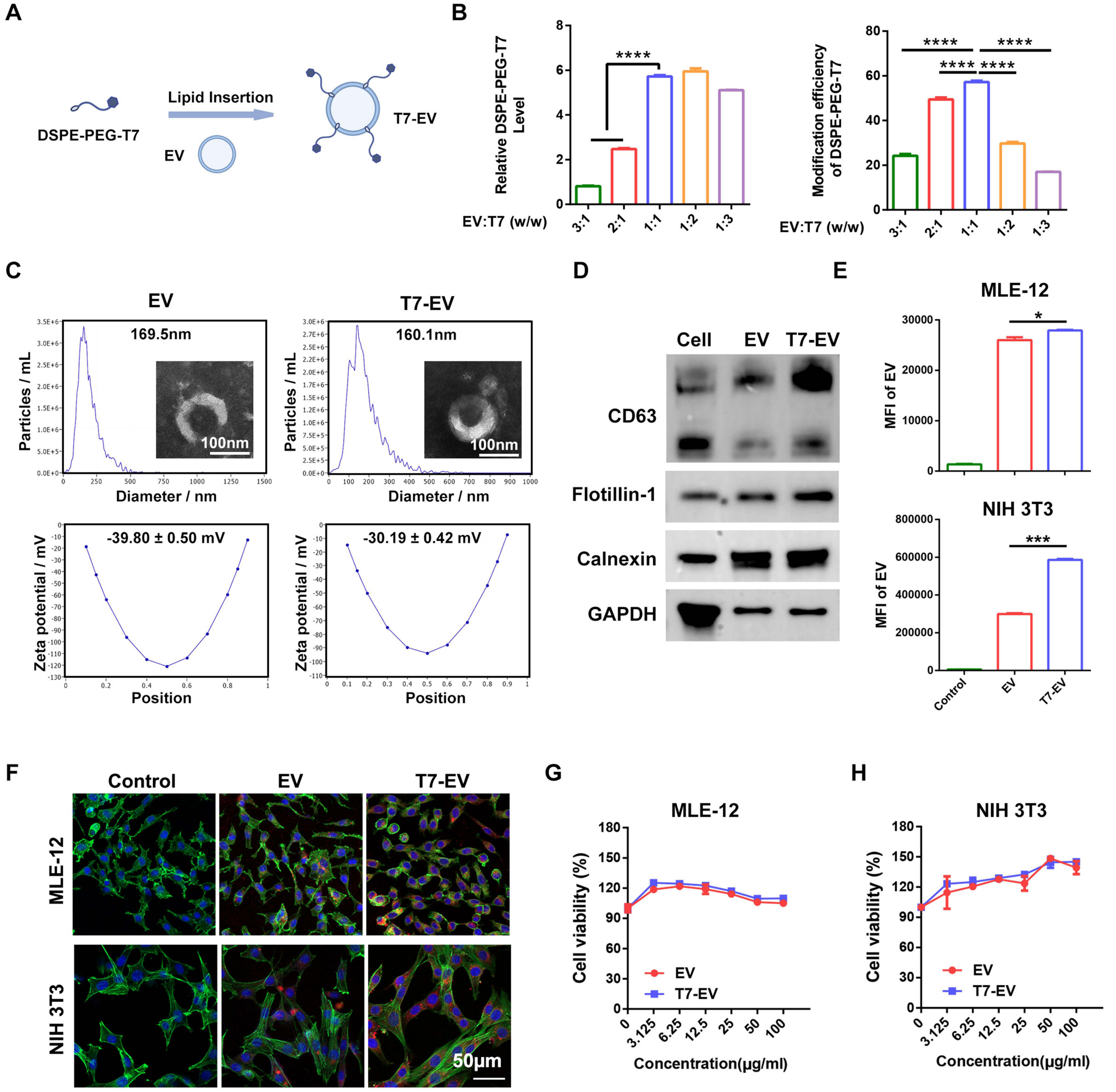

Figure 2 Engineering and characterization of T7-EV. (**A**) Schematic illustration of T7 peptide modification on EV surface via lipid insertion. (**B**) T7 modification efficiency. (**C**) TEM images showing the morphology of EVs and T7-EV; NTA analysis of particle size and Zeta potential. (**D**) Western blot analysis of marker proteins in EV and T7-EV. (**E**) Flow cytometry analysis of EV and T7-EV uptake by MLE-12 and NIH 3T3 cells. (**F**) Confocal microscopy images showing the cellular uptake of EVs and T7-EV by MLE-12 and NIH 3T3 cells. (**G**) CCK-8 assay evaluating the cytotoxicity of EVs and T7-EV on MLE-12 and (**H**) NIH 3T3 cells. Data are presented as the mean ± SD. $^{*}P < 0.05$, $^{***}P < 0.001$, $^{****}P < 0.0001$.

respectively, and zeta potentials of –39.80 ± 0.50 mV and –30.19 ± 0.42 mV (Figure 2C). Western blot analysis confirmed the expression of EV marker proteins including CD63, Flotillin-1, and Calnexin, consistent with previously reported extrusion-based EV, while the intracellular marker GAPDH was not detected (Figure 2D), indicating that T7 modification via lipid insertion does not alter the fundamental physical characteristics of EV.

Next, the uptake of DIR-labeled EV and T7-EV by MLE-12 and NIH 3T3 cells was evaluated using flow cytometry and confocal microscopy. The results demonstrated that although both EV and T7-EV were efficiently internalized, the intracellular fluorescence intensity was significantly higher in the T7-EV group, suggesting enhanced uptake (Figure 2E and F, S5B and C). Furthermore, cell viability assays showed no significant cytotoxicity in MLE-12 or NIH 3T3 cells after treatment with EVs or T7-EV, indicating good biocompatibility and that T7 modification did not introduce additional toxicity (Figure 2G and H).

Intracellular Behavior of T7-EV/siRNA

The high cellular uptake efficiency and excellent biocompatibility of EV make them promising carriers for siRNA delivery. siRNA was loaded into EV by electroporation, yielding EV+siRNA complexes that retained the characteristic cup-shaped morphology, with an average diameter of 170.9 nm and a zeta potential of –43.06 ± 1.00 mV. Western blot confirmed the presence of EV markers CD63, Flotillin-1, and Calnexin, with no detectable alterations in physical properties after siRNA loading (Figure S6A-B).

Compared to the commercial transfection reagent Lipo2000, EV exhibited negligible cytotoxicity in MLE-12 and NIH 3T3 cells at concentrations up to 100 µg/mL, indicating superior biocompatibility (Figure S6C). Flow cytometry revealed that the uptake efficiency of Naked-siRNA, Lipo+siRNA, and EV+siRNA by MLE-12 cells was 10.61 ± 2.73%, 41.84 ± 2.59%, and 86.26 ± 1.44%, respectively. The corresponding mean fluorescence intensities (MFI) of Cy3-siRNA were 47806 ± 2959, 107,946 ± 6664, and 183017 ± 173,645 (Figure S7A). Similarly, NIH 3T3 cells showed uptake efficiencies of 2.48 ± 0.43%, 60.17 ± 5.00%, and 67.15 ± 1.09%, with Cy3-siRNA MFI values of 22653 ± 1794, 75,762 ± 8943, and 110510 ± 1042, respectively (Figure S7B). Confocal microscopy further confirmed enhanced red fluorescence signals in EV+siRNA-treated cells, demonstrating superior delivery capability in both cell lines (Figure S7C).

Using the same protocol, we prepared T7-EV/siRNA complexes. Based on the standard curve of Cy3-siRNA, the loading efficiencies of EV/siRNA and T7-EV/siRNA were calculated as 27.69 ± 1.01% and 29.45 ± 1.71%, respectively (Figure S8A). Compared to EV/siRNA, T7-EV/siRNA showed significantly enhanced delivery to recipient MLE-12 and NIH 3T3 cells, as evidenced by increased uptake efficiency and elevated intracellular Cy3-siRNA fluorescence intensity (Figure 3A–D and S8B–C). To validate that the enhanced uptake was mediated via TFRC, MLE-12 and NIH 3T3 cells were pretreated with different concentrations of transferrin for 2 h. At 1.25 mg/mL, transferrin significantly inhibited T7-EV/Cy3-siRNA uptake, confirming TFRC-mediated internalization (Figure 3E and F). Furthermore, confocal imaging showed clear colocalization between T7-EV/Cy3-siRNA and TFRC on both cell types, consistent with flow cytometry results (Figure 3G and H). To exert gene-silencing effects, T7-EV/Cy3-siRNA complexes must escape from the lysosome and release therapeutic siRNA into the cytoplasm after cellular uptake. Therefore, we evaluated the intracellular localization of T7-EV/Cy3-siRNA in MLE-12 and NIH 3T3 cells at different time points. Confocal microscopy revealed pronounced colocalization between siRNA and lysosomes at 8 h post-treatment, which was significantly reduced at 24 h (Figure 3I and J).

We also evaluated the stability of T7-EV/siTGF-β1 under different storage conditions, which is critical for its therapeutic application. T7-EV/siTGF-β1 complexes showed a significant increase in particle size during storage at room temperature, while their size and zeta potential remained largely stable under low-temperature conditions (4 °C, −20 °C, and −80 °C), consistent with prior studies demonstrating the superiority of low-temperature storage for maintaining EV stability (Figure S9A-B).[35]

T7-EV/siTGF-β1 Attenuates Bleomycin-Induced Ferroptosis in MLE-12 Cells

The inhibitory effect of T7-EV/siTGF-β1 on bleomycin-induced ferroptosis was evaluated in MLE-12 cells. Following bleomycin exposure, cells were treated with PBS, siTGF-β1, T7-EV/siNC, or T7-EV/siTGF-β1. CCK-8 analysis showed that both T7-EV/siNC and T7-EV/siTGF-β1 significantly rescued bleomycin-induced loss of cell viability, restoring viability to 116.9 ± 12.75% and 120.7 ± 7.10%, respectively (Figure 4A). These treatments also markedly reduced intracellular Fe^{2+} levels to 64705 ± 6810 and 69572 ± 3991, respectively (Figure 4B). In contrast, PBS and siTGF-β1 alone failed to produce

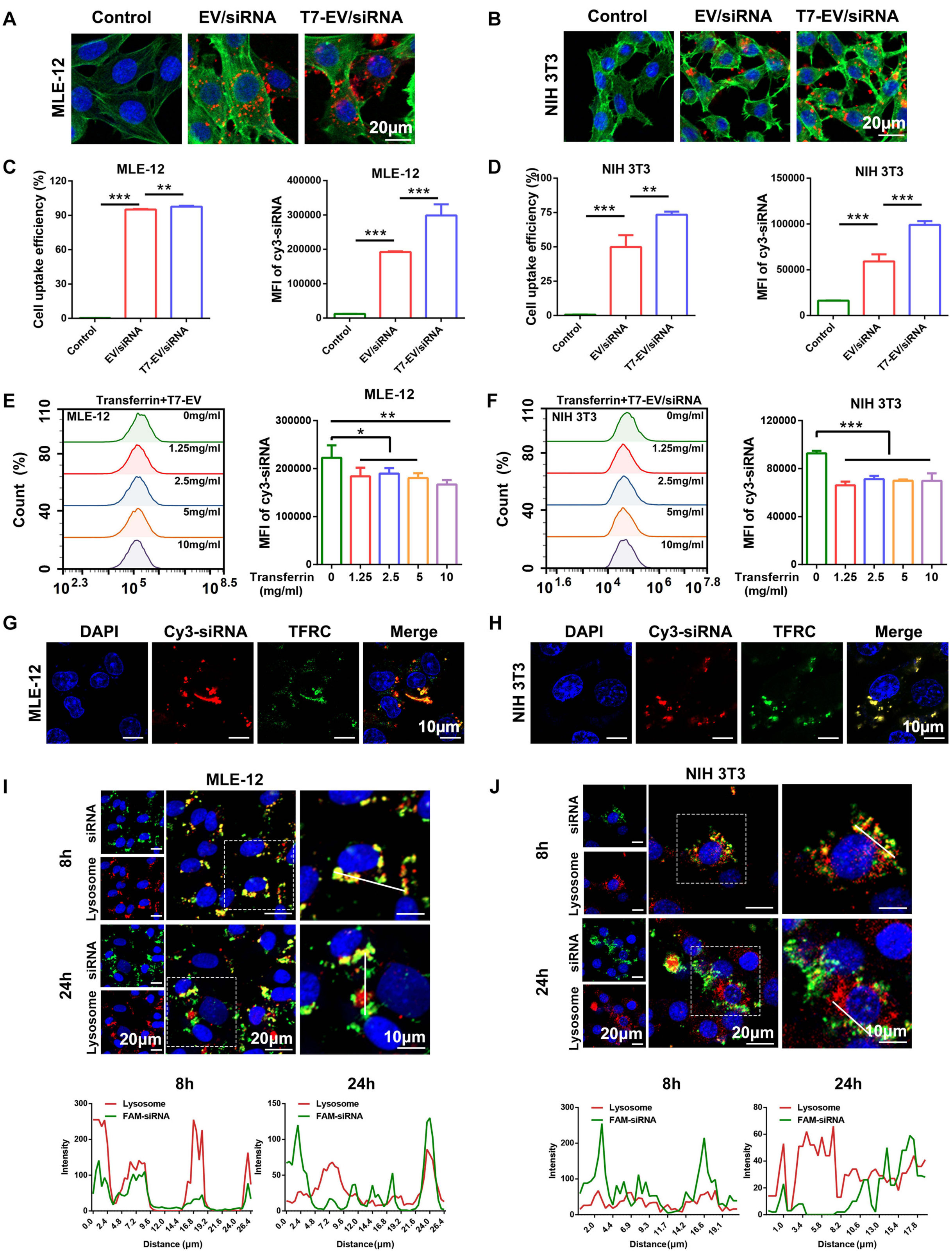

Figure 3 Targeted delivery of siRNA via T7-EV to TFRC-expressing cells. (**A**) Representative confocal microscopy images showing the uptake of EV/Cy3-siRNA and T7-EV /Cy3-siRNA by MLE-12 (**B**) and NIH 3T3 cells after 6 h of incubation. (**C**) Flow cytometry analysis of the uptake efficiency and mean fluorescence intensity (MFI) of Cy3-siRNA delivered by EV or T7-EV in MLE-12 (**D**) and NIH 3T3 cells. (**E**) Quantification of T7-EV/Cy3-siRNA uptake in MLE-12 (**F**) and NIH 3T3 cells pretreated with various concentrations of transferrin (0, 1.25, 2.5, 5.0, and 10.0 mg/mL) for 2 h. (**G**) Representative confocal images showing the colocalization of T7-EV/Cy3-siRNA (red) with TFRC (green) in MLE-12 (**H**) and NIH 3T3 cells after 6 h of incubation. (**I**) Confocal microscopy images depicting the colocalization of T7-EV/FAM-siRNA (green) with lysosomes (red) in MLE-12 (**J**) and NIH 3T3 cells at 8 and 24 h post-treatment. Data are presented as the mean ± SD. *P < 0.05, **P < 0.01, ***P < 0.001.

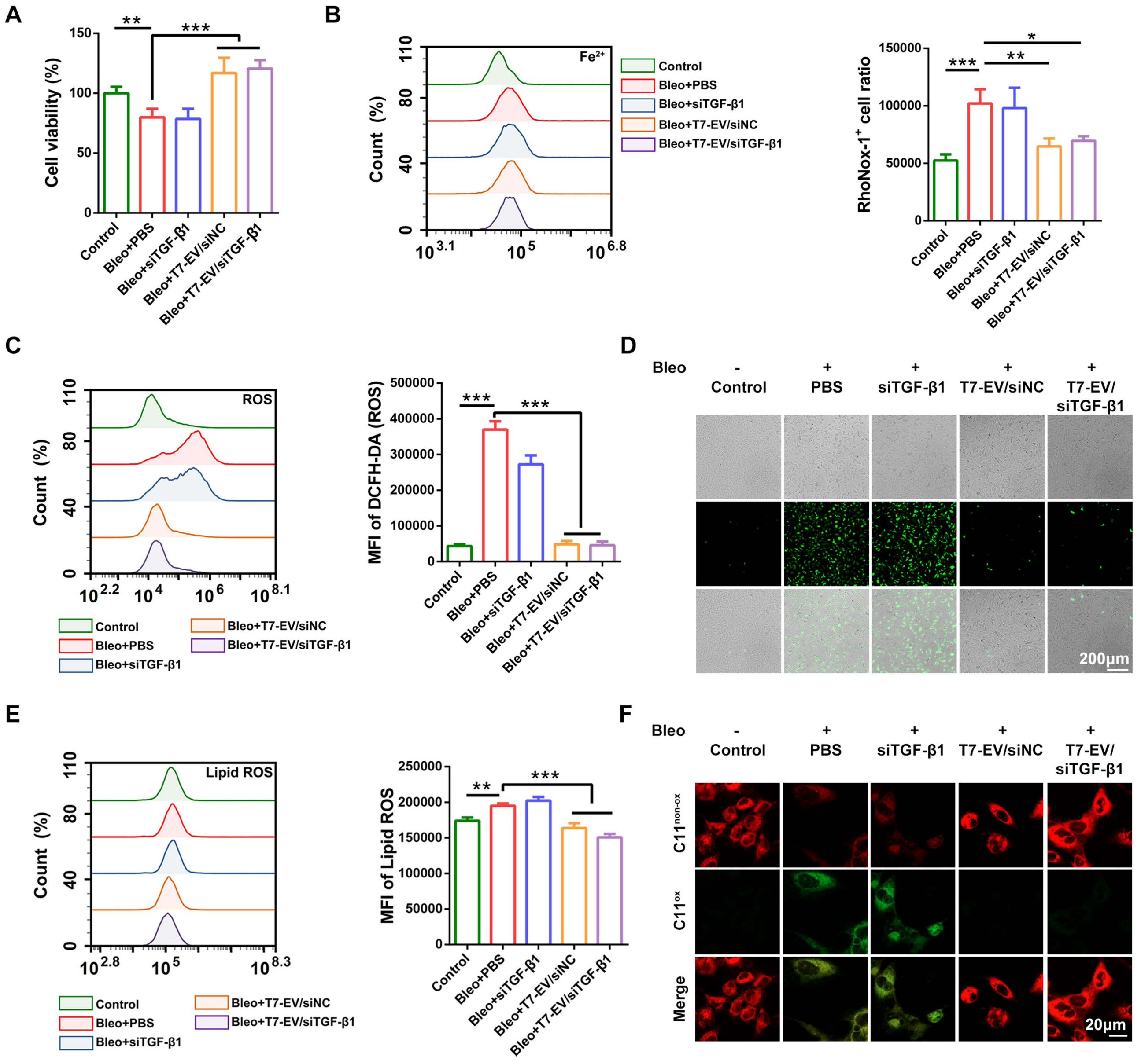

Figure 4 In vitro inhibition of ferroptosis by T7-EV/siTGF-β1. (**A**) Cell viability of MLE-12 cells after 48 h of various treatments was assessed using the CCK-8 assay. (**B**) Intracellular Fe^{2+} levels were measured by flow cytometry after 48 h of treatment. (**C**) Flow cytometric analysis and (**D**) fluorescence microscopy were used to evaluate ROS levels in MLE-12 cells stained with DCFH-DA probe after 48 h. (**E**) Flow cytometry and (**F**) confocal microscopy images showing lipid peroxidation levels in MLE-12 cells labeled with C11-BODIPY after 48 h of different treatments. Data are presented as the mean ± SD. *P < 0.05, **P < 0.01, ***P < 0.001.

comparable effects. Moreover, T7-EV/siNC and T7-EV/siTGF-β1 effectively attenuated oxidative stress induced by bleomycin, reducing ROS levels to 48579 ± 9157 and 45778 ± 10611, respectively (Figure 4C and D), and lipid peroxidation to 163715 ± 6852 and 150597 ± 4839, respectively (Figure 4E and F). No significant reduction in ROS or lipid peroxidation was observed in the PBS or siTGF-β1 groups. Collectively, these results suggest that T7-EV retain the antioxidant and anti-ferroptotic properties of their parental cells, and these functions remain unaffected after electroporation-mediated loading of siNC or siTGF-β1.

T7-EV/siTGF-β1 Suppresses TGF-β1 Expression and Fibroblast Activation

The inhibitory effect of T7-EV/siTGF-β1 on TGF-β1 protein expression was evaluated in MLE-12 cells. In the absence of bleomycin stimulation, treatment with T7-EV/siTGF-β1 for 48 h significantly reduced the expression of TGF-β1 protein in MLE-12 cells (Figure 5A). Upon bleomycin stimulation, TGF-β1 expression was markedly upregulated, while co-treatment with T7-EV/siTGF-β1 effectively reversed this increase (Figure 5B).

To assess the downstream impact, CM from bleomycin-stimulated MLE-12 cells treated with PBS, siTGF-β1, T7-EV/siNC, or T7-EV/siTGF-β1 were applied to NIH 3T3 cells. Transwell assays revealed that the T7-EV/siTGF-β1 group exhibited significantly reduced pro-migratory effects, with only 42 ± 3 cells migrating to the lower chamber, compared to 70 ± 3 in the PBS group, 69 ± 3 in the siTGF-β1 group, and 66 ± 3 in the T7-EV/siNC group (Figure 5C). Consistent with these findings, immunofluorescence staining demonstrated markedly lower expression of α-SMA and Collagen I in NIH 3T3 cells treated with the T7-EV/siTGF-β1-CM compared to the other groups (Figure 5D). Together, these results indicate that T7-EV/siTGF-β1 effectively suppresses TGF-β1 protein expression and secretion in bleomycin-stimulated MLE-12 cells, thereby potentially limiting subsequent fibroblast activation. Moreover, following internalization by NIH 3T3 cells, T7-EV/siTGF-β1 effectively downregulated intracellular TGF-β1 protein expression (Figure 5E) and directly impaired fibroblast migratory capacity, reducing the number of migrated cells from 112.30 ± 7.64 to 65.67 ± 5.51 (Figure 5F).

Inhaled T7-EV/siTGF-β1 Alleviates Bleomycin-Induced Pulmonary Fibrosis in vivo

Finally, the therapeutic efficacy of T7-EV/siTGF-β1 was evaluated in a murine model of pulmonary fibrosis. To assess organ distribution following inhalation delivery, ex vivo fluorescence imaging was first performed. The results demonstrated that aerosolized T7-EV/Cy5-siRNA was predominantly enriched in the lungs, with negligible signal detected in the heart, liver, spleen, or kidneys. This localized delivery approach effectively enhanced pulmonary targeting, improved bioavailability, and minimized off-target exposure, thereby potentially reducing systemic toxicity (Figure S10A).

Pulmonary fibrosis was induced by intratracheal instillation of bleomycin, followed by local administration of T7-EV/siTGF-β1 via aerosol inhalation. Mice began receiving treatment on Day 3 post-induction (Figure 6A). T7-EV/siTGF-β1 treatment significantly improved survival rates compared to PBS, siTGF-β1, and T7-EV/siNC groups (Figure 6B), and markedly attenuated weight loss during disease progression (Figure 6C). On Day 21, lung tissues were harvested for histological analysis. HE and Masson staining were performed to assess fibrosis severity. Quantitative analysis of Masson-positive areas revealed that T7-EV/siTGF-β1 treatment significantly reduced fibrotic area to 5.02 ± 0.63%, in contrast to PBS (36.46 ± 5.28%), siTGF-β1 (33.55 ± 6.84%), and T7-EV/siNC (16.12 ± 1.32%) groups (Figure 6D and E). Notably, T7-EV/siNC alone also led to a moderate reduction in fibrosis, suggesting that T7-EV retains intrinsic biological activity. These findings indicate that T7-EV/siTGF-β1 exerts synergistic anti-ferroptotic and anti-fibrotic effects, achieving superior therapeutic outcomes. In contrast, naked siTGF-β1 failed to exert therapeutic effects, likely due to poor cellular uptake or rapid enzymatic degradation in vivo.

Immunohistochemistry further supported these findings. TGF-β1 expression in lung tissues was significantly suppressed in the T7-EV/siTGF-β1 group (3.49 ± 0.72%) compared to all other groups (Figure 6F). α-SMA staining revealed that T7-EV/siTGF-β1 markedly inhibited fibroblast activation, with a positive area of only 3.17 ± 0.80% (Figure 6G). EPPB staining, indicative of iron accumulation, showed that T7-EV/siTGF-β1 treatment significantly reduced iron deposition to 5.17 ± 0.79%, compared to PBS (15.50 ± 1.21%), siTGF-β1 (12.13 ± 3.00%), and T7-EV/siNC (11.49 ± 2.33%) groups (Figure 6H). Moreover, DHE staining revealed that both T7-EV/siNC and T7-EV/siTGF-β1 substantially decreased ROS levels, as evidenced by reduced red fluorescence intensity, highlighting their antioxidative potential.

Lastly, HE staining of major organs (heart, liver, spleen, kidney) was conducted to preliminarily evaluate in vivo safety. No overt histopathological abnormalities were observed, indicating that the treatment was well tolerated (Figure S11A).

Discussion

Pulmonary fibrosis is a complex pathological condition characterized by multi-factorial etiologies and involving various cell types and signaling pathways. Among early events in fibrosis, injury to alveolar epithelial cells (AECs) plays a pivotal role by releasing profibrotic cytokines,[2] which activate fibroblasts and promote excessive collagen deposition and ECM remodeling.

In this study, we focused on ferroptosis, a newly recognized form of regulated cell death, and its role in the development of pulmonary fibrosis.[36–38] We observed that bleomycin-induced ferroptosis in AECs was accompanied by a marked upregulation of TGF-β1. Notably, treatment with the classical ferroptosis inhibitor Fer-1 effectively reversed

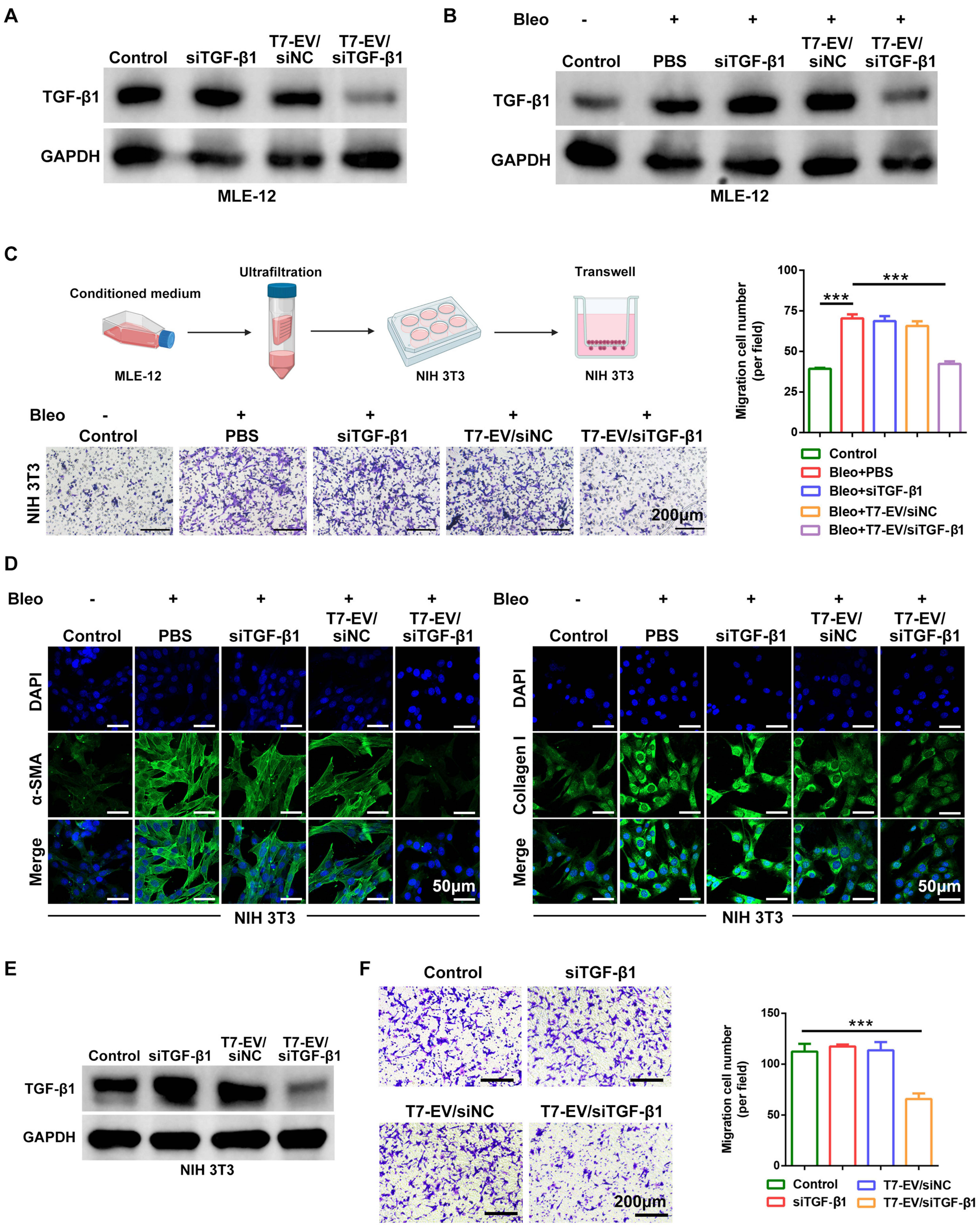

Figure 5 Anti-fibrotic effects of T7-EV/siTGF-β1 in vitro. (**A**) Western blot analysis of TGF-β1 protein expression in MLE-12 cells after 48 h treatment with Control, siTGF-β1, T7-EV/siNC, or T7-EV/siTGF-β1. (**B**) Western blot showing the effect of different treatments on bleomycin-induced upregulation of TGF-β1 in MLE-12 cells after 48 h. (**C**) Transwell assay evaluating the migration of NIH 3T3 cells induced by CM collected from MLE-12 cells treated under different conditions. (**D**) Immunofluorescence staining of α-SMA and Collagen I expression in NIH 3T3 cells following stimulation with the respective CM. (**E**) Western blot analysis of TGF-β1 protein expression in NIH 3T3 cells after 48 h treatment with Control, siTGF-β1, T7-EV/siNC, or T7-EV/siTGF-β1. (**F**) Transwell assay evaluating the migration of NIH 3T3 cells after 48 h treatment with Control, siTGF-β1, T7-EV/siNC, or T7-EV/siTGF-β1. Data are presented as the mean ± SD. ***P < 0.001.

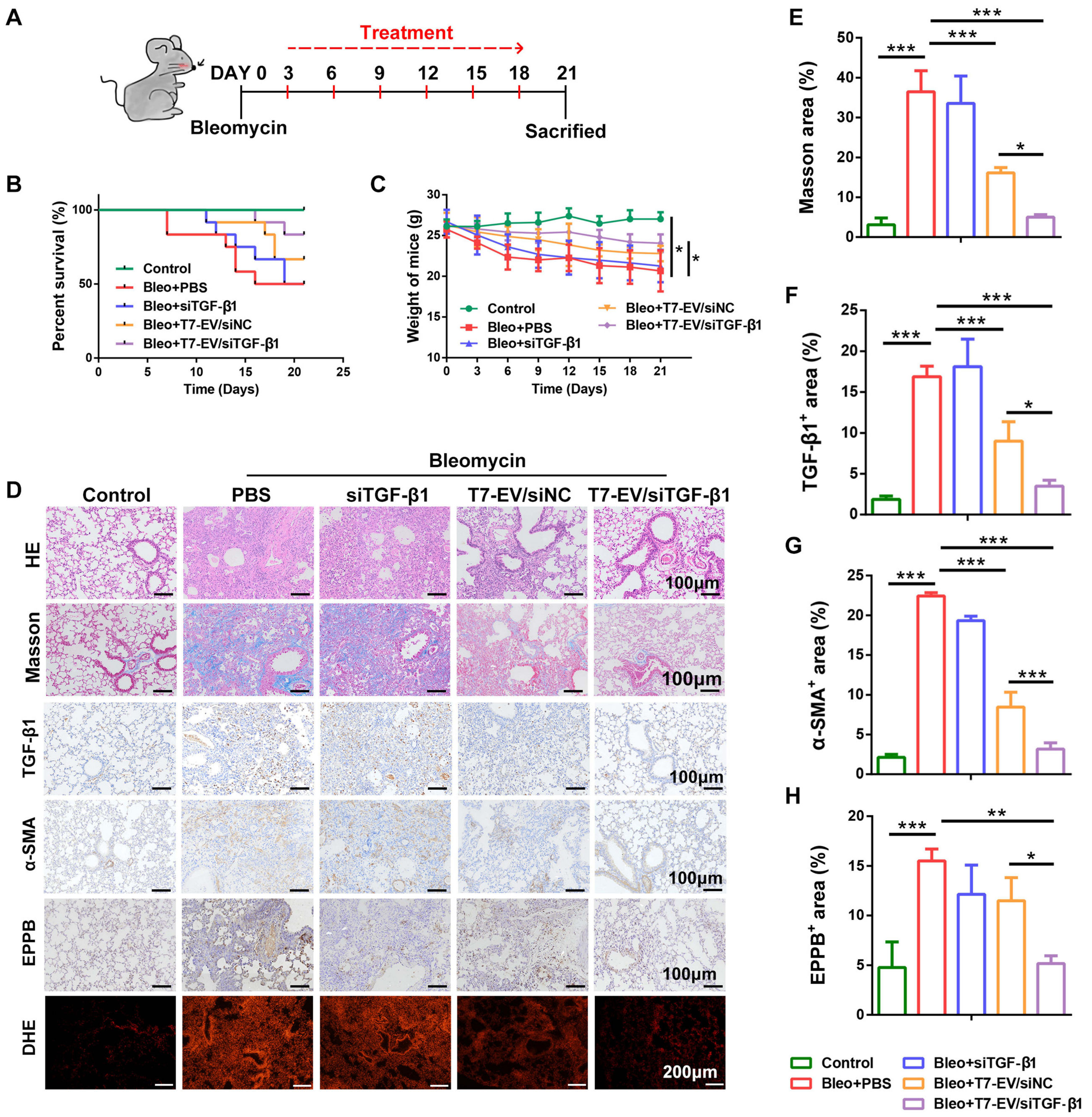

Figure 6 In vivo therapeutic effect of T7-EV/siTGF-β1 in a bleomycin-induced mouse model of pulmonary fibrosis. (**A**) Schematic illustration of the bleomycin-induced pulmonary fibrosis model and treatment schedule in mice. (**B**) Survival curves. (**C**) Body weight changes during the treatment period. (**D**) Representative images of lung sections stained with HE, Masson's trichrome, TGF-β1 and α-SMA immunohistochemistry (IHC), enhanced Prussian blue (EPPB), and DHE fluorescence. (**E**) Quantitative analysis of Masson's trichrome staining. (**F**) Quantification of TGF-β1 IHC staining. (**G**) Quantification of α-SMA IHC staining. (**H**) Quantification of EPPB staining. Data are presented as the mean ± SD. *$P < 0.05$, **$P < 0.01$, ***$P < 0.001$.

this effect, significantly reducing TGF-β1 expression. Furthermore, conditioned media from bleomycin-injured epithelial cells enhanced fibroblast migration, while Fer-1 treatment abolished this pro-migratory effect.[39] These findings support two key conclusions: first, that ferroptosis plays a critical role in the pathogenesis of pulmonary fibrosis; and second, that ferroptosis may contribute to fibrogenesis through paracrine signaling, highlighting it as a promising therapeutic target. However, the translational potential of current ferroptosis inhibitors is limited by their poor aqueous solubility, rapid metabolic degradation, and low bioavailability, highlighting the urgent need for novel treatment strategies capable of achieving targeted, stable, and efficient delivery.[40]

https://doi.org/10.2147/IJN.S568106

Iron uptake is central to ferroptosis execution, and the transferrin receptor (TFRC), a key mediator of cellular Fe^{3+} import,[41] was found to be significantly upregulated in AECs during the early stages of fibrosis. As fibrosis progressed, TFRC expression gradually declined, likely as a consequence of progressive epithelial loss. Interestingly, TGF-β1 also moderately upregulated TFRC expression in fibroblasts, consistent with previous reports.[23] These stage-dependent expression patterns underscore the context-specific role of TFRC in fibrotic lungs. Notably, ferroptosis has been recognized as a potential therapeutic target in cancer. In lung cancer, ferroptosis is generally considered a tumor-suppressive mechanism, particularly in early and treatment-sensitive stages, where its induction can limit cancer cell survival.[42] Accordingly, broad inhibition of ferroptosis may theoretically compromise antitumor defenses. In contrast, TGF-β1 signaling plays a pro-tumorigenic role during cancer progression by promoting epithelial–mesenchymal transition, immune suppression, and tumor–stroma interactions, especially in advanced stages.[43] Therefore, the biological consequences of inhibiting ferroptosis and TGF-β1 signaling are fundamentally different in lung cancer and must be interpreted in a stage-specific manner. In this context, the transient upregulation of TFRC during early fibrotic progression may define a critical therapeutic window, in which TFRC-targeted strategies enable selective delivery of therapeutics to fibrotic lungs, aiming to inhibit ferroptosis and subsequent fibroblast activation, while minimizing unintended interference with ferroptosis-dependent antitumor mechanisms in cancer. In potential clinical applications, such strategies should be implemented in conjunction with appropriate diagnostic evaluation to exclude coexisting or latent lung malignancies, thereby improving patient stratification and therapeutic safety.

Building upon these insights, we developed a novel targeted delivery system: T7 peptide-functionalized extracellular vesicles (T7-EV) for the pulmonary delivery of siRNA against TGF-β1 (siTGF-β1). This platform incorporates several key design features: (1) Human umbilical cord mesenchymal stem cell-derived EVs (HucMSC-EVs) were selected as the delivery vehicle due to their low immunogenicity, abundant source, and innate regenerative capacity, which have made them widely used in the treatment of various tissue injuries. HucMSC-EVs alone were able to attenuate bleomycin-induced ferroptosis in AECs, likely via antioxidant and cytoprotective mechanisms;[44] (2) EV surface modification with DSPE-PEG2000-T7 via hydrophobic insertion enabled TFRC-targeted delivery without the use of toxic chemical cross-linkers, thereby enhancing safety and clinical applicability; (3) Efficient loading of siTGF-β1 was achieved using electroporation,[45] endowing the platform with anti-fibrotic properties through targeted silencing of TGF-β1 expression; (4) The natural phospholipid bilayer of EVs confers superior mechanical stability, protecting siRNA from shear degradation during nebulization. This makes EVs particularly suitable for pulmonary delivery via inhalation. Compared to conventional vectors such as cationic liposomes, EVs are derived from endogenous sources, exhibit lower cytotoxicity and immunogenicity, and are better suited for long-term pulmonary administration.

In vitro studies confirmed that T7-EV/siTGF-β1 was efficiently internalized by both AECs (MLE-12) and fibroblasts (NIH 3T3), significantly suppressing ferroptosis and fibrotic activation. In vivo, nebulized administration of T7-EV /siTGF-β1 led to preferential lung accumulation, effectively alleviating bleomycin-induced pulmonary fibrosis in mice. This therapeutic effect was evidenced by reduced expression of TGF-β1 and the fibroblast marker α-SMA, decreased iron overload and reactive oxygen species (ROS) levels, and improved histological architecture. Importantly, the platform exhibited favorable biocompatibility and safety.

Compared with currently reported EV–based or siRNA-mediated anti-fibrotic systems, the T7-EV platform exhibits several mechanistic and translational advantages. Native or unmodified EVs used in prior studies primarily rely on passive biodistribution and often demonstrate suboptimal accumulation within fibrotic lesions, partly due to the heterogeneous and dynamically remodeled extracellular matrix in IPF.[46,47] Chemical or ligand-based modifications have improved targeting to some extent, yet many existing strategies focus on single-cell populations, typically fibroblasts, while overlooking the simultaneous involvement of epithelial cells in ferroptosis-mediated injury. For siRNA-based therapeutics, synthetic nanocarriers such as liposomes, polymers, or lipid nanoparticles have been employed to enhance stability and delivery.[48,49] However, these carriers may elicit immunogenicity, induce off-target tissue accumulation, or undergo rapid clearance, thereby constraining the therapeutic window.[50]

T7-EVs integrate TFRC-mediated active targeting with a biocompatible vesicle system and enable efficient siRNA delivery to epithelial cells and fibroblasts, two key cell types involved in fibrotic progression. This coordinated targeting allows simultaneous regulation of ferroptosis and fibroblast activation and provides a more integrated therapeutic approach than systems that focus on a single pathway. Nebulized administration further improves lung-specific deposition and reduces systemic exposure. However, issues such as scalable production, long-term stability, and optimization of cargo retention remain important considerations for future development.

Building on these mechanistic and translational advantages, the safety profile of T7-EV/siTGF-β1 is also an important consideration. Ferroptosis plays critical roles in cellular homeostasis, and excessive or systemic inhibition could theoretically interfere with tumor-suppressive mechanisms. Localized and short-term administration via aerosolized T7-EV/siTGF-β1 is expected to minimize systemic exposure, providing focused therapeutic effects within the lung microenvironment. Future preclinical and clinical studies are required to evaluate long-term biosafety, including potential tumorigenic risks, to ensure efficacy without compromising safety.

In summary, our study highlights a previously unrecognized link between epithelial ferroptosis and TGF-β1-mediated fibrogenesis, and identifies TFRC as a receptor abnormally upregulated during the early to intermediate stages of pulmonary fibrosis. Based on this, we propose a novel TFRC-targeted EV delivery system for siTGF-β1 as a dual-action therapeutic strategy. By simultaneously blocking ferroptosis and fibroblast activation, this inhalable nanoplatform offers a promising solution for early intervention in pulmonary fibrosis. Our work not only expands the mechanistic understanding of disease pathogenesis but also establishes a clinically translatable platform for precise and effective therapy.

Conclusions

In summary, we developed TFRC-targeted extracellular vesicles (T7-EV) to deliver siTGF-β1 specifically to fibrotic lung tissue. These engineered vesicles effectively inhibited bleomycin-induced ferroptosis and fibroblast activation both in vitro and in vivo. T7-EV demonstrated enhanced cellular uptake, excellent biocompatibility, and precise lung targeting after inhalation. Our findings provide a novel dual-function therapeutic strategy combining anti-ferroptotic and anti-fibrotic effects, offering promising potential for the treatment of pulmonary fibrosis and advancing cell-free nanotherapy for respiratory diseases.

Clinical Sample Collection

The use of lung tissues was approved by the Ethics Committee of the Sichuan Provincial People's Hospital, School of Medicine, University of Electronic Science and Technology of China. All procedures involving human participants were conducted in accordance with the Declaration of Helsinki. Written informed consent was obtained from all participants. Ethics approval number: EC-2025-305.

Data Sharing Statement

The majority of the data obtained and the materials used are presented in this publication. Additional data or materials will be provided upon reasonable request and the signing of a material transfer agreement. Data is available from the corresponding author.

All animal procedures were approved and controlled by the Institutional Animal Care and Treatment Committee of Sichuan University and conducted according to the Animal Care and Use Guidelines of Sichuan University.

Ethics Approval and Consent to Participate

All animal procedures were approved and controlled by the Institutional Animal Care and Treatment Committee of Sichuan University and conducted according to the Animal Care and Use Guidelines of Sichuan University.

Author Contributions

All authors made a significant contribution to the work reported, whether that is in the conception, study design, execution, acquisition of data, analysis and interpretation, or in all these areas; took part in drafting, revising or critically reviewing the article; gave final approval of the version to be published; have agreed on the journal to which the article has been submitted; and agree to be accountable for all aspects of the work.

Funding

This work was supported by Chengdu Hi-Tech Medical Association (No. 2024009).

Disclosure

The authors declare that they have no competing interests in this work.

References

1. Wolters PJ, Collard HR, Jones KD. Pathogenesis of idiopathic pulmonary fibrosis. *Annu Rev Pathol*. 2014;9:157–179. doi:10.1146/annurev-pathol-012513-104706
2. Richeldi L, Collard HR, Jones MG. Idiopathic pulmonary fibrosis. *Lancet*. 2017;389(10082):1941–1952. doi:10.1016/S0140-6736(17)30866-8
3. Noble PW, Albera C, Bradford WZ, et al. Pirfenidone in patients with idiopathic pulmonary fibrosis (CAPACITY): two randomised trials. *Lancet*. 2011;377(9779):1760–1769. doi:10.1016/S0140-6736(11)60405-4
4. Richeldi L, du Bois RM, Raghu G, et al. Efficacy and safety of nintedanib in idiopathic pulmonary fibrosis. *N Engl J Med*. 2014;370(22):2071–2082. doi:10.1056/NEJMoa1402584
5. Cottin V, Martinez FJ, Jenkins RG, et al. Safety and tolerability of nintedanib in patients with progressive fibrosing interstitial lung diseases: data from the randomized controlled INBUILD trial. *Respir Res*. 2022;23(1):85.
6. Ghazipura M, Mammen MJ, Herman DD, et al. Nintedanib in progressive pulmonary fibrosis: a systematic review and meta-analysis. *Ann Am Thorac Soc*. 2022;19(6):1040–1049.
7. King TE, Bradford WZ, Castro-Bernardini S, et al. A Phase 3 trial of pirfenidone in patients with idiopathic pulmonary fibrosis. *N Engl J Med*. 2014;370(22):2083–2092.
8. Ornatowski W, Lu Q, Yegambaram M, et al. Complex interplay between autophagy and oxidative stress in the development of pulmonary disease. *Redox Biol*. 2020;36:101679.
9. Hernandez-Gonzalez F, Faner R, Rojas M, Agustí A, Serrano M, Sellarés J. Cellular senescence in lung fibrosis. *Int J Mol Sci*. 2021;22(13):7012.
10. Jaeger B, Schupp JC, Plappert L, et al. Airway basal cells show a dedifferentiated KRT17 highPhenotype and promote fibrosis in idiopathic pulmonary fibrosis. *Nat Commun*. 2022;13(1):5637. doi:10.1038/s41467-022-33193-0
11. Thannickal VJ, Toews GB, White ES, Lynch JP, Martinez FJ. Mechanisms of pulmonary fibrosis. *Annu Rev Med*. 2004;55:395–417. doi:10.1146/annurev.med.55.091902.103810
12. Morse C, Tabib T, Sembrat J, et al. Proliferating SPP1/MERTK-expressing macrophages in idiopathic pulmonary fibrosis. *Eur Respir J*. 2019;54(2):1802441. doi:10.1183/13993003.02441-2018
13. Selvarajah B, Azuelos I, Anastasiou D, Chambers RC. Fibrometabolism-An emerging therapeutic frontier in pulmonary fibrosis. *Sci Signal*. 2021;14(697). doi:10.1126/scisignal.aay1027
14. Bueno M, Calyeca J, Rojas M, Mora AL. Mitochondria dysfunction and metabolic reprogramming as drivers of idiopathic pulmonary fibrosis. *Redox Biol*. 2020;33:101509. doi:10.1016/j.redox.2020.101509
15. Dixon SJ, Lemberg KM, Lamprecht MR, et al. Ferroptosis: an iron-dependent form of nonapoptotic cell death. *Cell*. 2012;149(5):1060–1072. doi:10.1016/j.cell.2012.03.042
16. Yang WS, Stockwell BR. Ferroptosis: Death by lipid peroxidation. *Trends Cell Biol*. 2016;26(3):165–176. doi:10.1016/j.tcb.2015.10.014
17. Xu W, Deng H, Hu S, et al. Role of ferroptosis in lung diseases. *J Inflamm Res*. 2021;14:2079–2090. doi:10.2147/JIR.S307081
18. Sindrilaru A, Peters T, Wieschalka S, et al. An unrestrained proinflammatory M1 macrophage population induced by iron impairs wound healing in humans and mice. *J Clin Invest*. 2011;121(3):985–997. doi:10.1172/JCI44490
19. Burgy O, Mayr CH, Schenesse D, et al. Fibroblast-derived extracellular vesicles contain SFRP1 and mediate pulmonary fibrosis. *JCI Insight*. 2024;9(18). doi:10.1172/jci.insight.168889
20. Li Y, Du X, Hu Y, et al. Iron-laden macrophage-mediated paracrine profibrotic signaling induces lung fibroblast activation. *Am J Physiol Cell Physiol*. 2024;327(4):C979–C993. doi:10.1152/ajpcell.00675.2023
21. Zhang W, Sun Z, Cheng W, et al. Impaired GPX4 activity elicits ferroptosis in alveolar type II cells promoting PHMG-induced pulmonary fibrosis development. *Ecotoxicol Environ Saf*. 2024;281:116680. doi:10.1016/j.ecoenv.2024.116680
22. Tomitsuka Y, Imaeda H, Ito H, et al. Gene deletion of long-chain acyl-CoA synthetase 4 attenuates xenobiotic chemical-induced lung injury via the suppression of lipid peroxidation. *Redox Biol*. 2023;66:102850. doi:10.1016/j.redox.2023.102850
23. Pei Z, Qin Y, Fu X, et al. Inhibition of ferroptosis and iron accumulation alleviates pulmonary fibrosis in a bleomycin model. *Redox Biol*. 2022;57:102509. doi:10.1016/j.redox.2022.102509
24. Border WA, Noble NA, Noble NA. Transforming growth factor beta in tissue fibrosis. *N Engl J Med*. 1994;331(19):1286–1292. doi:10.1056/NEJM199411103311907
25. Scarpellini C, Klejborowska G, Lanthier C, Hassannia B, Vanden Berghe T, Augustyns K. Beyond ferrostatin-1: a comprehensive review of ferroptosis inhibitors. *Trends Pharmacol Sci*. 2023;44(12):902–916. doi:10.1016/j.tips.2023.08.012
26. Zamanian MH, Norooznezhad AH, Hosseinkhani Z, et al. Human placental mesenchymal stromal cell-derived small extracellular vesicles as a treatment for severe COVID-19: a double-blind randomized controlled clinical trial. *J Extracell Vesicles*. 2024;13(7):e12492. doi:10.1002/jev2.12492
27. Akhlaghpasand M, Tavanaei R, Hosseinpoor M, et al. Safety and potential effects of intrathecal injection of allogeneic human umbilical cord mesenchymal stem cell-derived exosomes in complete subacute spinal cord injury: a first-in-human, single-arm, open-label, Phase I clinical trial. *Stem Cell Res Ther*. 2024;15(1):264. doi:10.1186/s13287-024-03868-0
28. Shi -M-M, Yang Q-Y, Monsel A, et al. Preclinical efficacy and clinical safety of clinical-grade nebulized allogenic adipose mesenchymal stromal cells-derived extracellular vesicles. *J Extracell Vesicles*. 2021;10(10):e12134. doi:10.1002/jev2.12134
29. Bai X, Zhao G, Chen Q, et al. Inhaled siRNA nanoparticles targeting IL11 inhibit lung fibrosis and improve pulmonary function post-bleomycin challenge. *Sci Adv*. 2022;8(25):eabn7162. doi:10.1126/sciadv.abn7162

30. Liu M, Hu S, Yan N, Popowski KD, Cheng K. Inhalable extracellular vesicle delivery of IL-12 mRNA to treat lung cancer and promote systemic immunity. *Nat Nanotechnol*. 2024;19(4):565–575. doi:10.1038/s41565-023-01580-3
31. Jiang AY, Witten J, Raji IO, et al. Combinatorial development of nebulized mRNA delivery formulations for the lungs. *Nat Nanotechnol*. 2024;19(3):364–375. doi:10.1038/s41565-023-01548-3
32. Kim G, Kim M, Lee Y, Byun JW, Hwang DW, Lee M. Systemic delivery of microRNA-21 antisense oligonucleotides to the brain using T7-peptide decorated exosomes. *J Control Release*. 2020;317:273–281. doi:10.1016/j.jconrel.2019.11.009
33. Tang J, Wang Q, Yu Q, et al. A stabilized retro-inverso peptide ligand of transferrin receptor for enhanced liposome-based hepatocellular carcinoma-targeted drug delivery. *Acta Biomater*. 2019;83:379–389. doi:10.1016/j.actbio.2018.11.002
34. Jang SC, Kim OY, Yoon CM, et al. Bioinspired exosome-mimetic nanovesicles for targeted delivery of chemotherapeutics to malignant tumors. *ACS Nano*. 2013;7(9):7698–7710. doi:10.1021/nn402232g
35. Wu J-Y, Li Y-J, Hu X-B, Huang S, Xiang D-X. Preservation of small extracellular vesicles for functional analysis and therapeutic applications: a comparative evaluation of storage conditions. *Drug Deliv*. 2021;28(1):162–170. doi:10.1080/10717544.2020.1869866
36. Yang L, Cao L-M, Zhang X-J, Chu B. Targeting ferroptosis as a vulnerability in pulmonary diseases. *Cell Death Dis*. 2022;13(7):649. doi:10.1038/s41419-022-05070-7
37. Yue D, Zhang Q, Zhang J, et al. Diesel exhaust PM2.5 greatly deteriorates fibrosis process in pre-existing pulmonary fibrosis via ferroptosis. *Environ Int*. 2023;171:107706. doi:10.1016/j.envint.2022.107706
38. Liu Y, Cheng D, Wang Y, et al. UHRF1-mediated ferroptosis promotes pulmonary fibrosis via epigenetic repression of GPX4 and FSP1 genes. *Cell Death Dis*. 2022;13(12):1070. doi:10.1038/s41419-022-05515-z
39. Skouta R, Dixon SJ, Wang J, et al. Ferrostatins inhibit oxidative lipid damage and cell death in diverse disease models. *J Am Chem Soc*. 2014;136(12):4551–4556. doi:10.1021/ja411006a
40. Zhang F, Xiang Y, Ma Q, Guo E, Zeng X. A deep insight into ferroptosis in lung disease: facts and perspectives. *Front Oncol*. 2024;14:1354859. doi:10.3389/fonc.2024.1354859
41. Hentze MW, Muckenthaler MU, Andrews NC. Balancing acts: molecular control of mammalian iron metabolism. *Cell*. 2004;117(3):285–297. doi:10.1016/S0092-8674(04)00343-5
42. Wu S, Zhu C, Tang D, Dou QP, Shen J, Chen X. The role of ferroptosis in lung cancer. *Biomark Res*. 2021;9(1):82. doi:10.1186/s40364-021-00338-0
43. Turati M, Mousset A, Issa N, Turtoi A, Ronca R. TGF-β mediated drug resistance in solid cancer. *Cytokine Growth Factor Rev*. 2023;71-72:54–65. doi:10.1016/j.cytogfr.2023.04.001
44. Yu Y, Wu T, Lu Y, et al. Exosomal thioredoxin-1 from hypoxic human umbilical cord mesenchymal stem cells inhibits ferroptosis in doxorubicin-induced cardiotoxicity via mTORC1 signaling. *Free Radic Biol Med*. 2022;193(Pt 1):108–121. doi:10.1016/j.freeradbiomed.2022.10.268
45. Lunavat TR, Jang SC, Nilsson L, et al. RNAi delivery by exosome-mimetic nanovesicles–Implications for targeting c-Myc in cancer. *Biomaterials*. 2016;102:231–238. doi:10.1016/j.biomaterials.2016.06.024
46. Zhu J, Wang S, Yang D, Xu W, Qian H. Extracellular vesicles: emerging roles, biomarkers and therapeutic strategies in fibrotic diseases. *J Nanobiotechnol*. 2023;21(1):164. doi:10.1186/s12951-023-01921-3
47. Amtil-Ouahdi I, Vergara F, Rio C, et al. EVs biodistribution and antifibrotic impact in aged lung fibrosis model. *Biofactors*. 2025;51(3):e70021. doi:10.1002/biof.70021
48. Cheng D, Wang Y, Li Z, et al. Liposomal UHRF1 siRNA shows lung fibrosis treatment potential through regulation of fibroblast activation. *JCI Insight*. 2022;7(22). doi:10.1172/jci.insight.162831
49. Moazzam M, Zhang M, Hussain A, Yu X, Huang J, Huang Y. The landscape of nanoparticle-based siRNA delivery and therapeutic development. *Mol Ther*. 2024;32(2):284–312.
50. Wang Y, Xuan W, Mao C, Liu Y. Inhalable nucleic acid therapeutics for chronic pulmonary disease: Progress, challenges, and prospects. *Acta Biomater*. 2025;204:187–204.